Tribology International 109 (2017) 258–273

Contents lists available at ScienceDirect

Tribology International

journal homepage: www.elsevier.com/locate/triboint

A coupled finite-volume CFD solver for two-dimensional elasto-hydrodynamic lubrication problems with particular application to rolling element bearings

A. Hajishafiee, A. Kadiric*, S. Ioannides, D. Dini

Tribology Group, Department of Mechanical Engineering, Imperial College London, London SW7 2AZ, UK

ARTICLE INFO

Keywords:
CFD
Fluid-solid interactions
Elasto-hydrodynamic lubrication (EHL)
Rolling element bearings

ABSTRACT

This paper describes a new computational fluid dynamics methodology for modelling elastohydrodynamic contacts. A finite-volume technique is implemented in the 'OpenFOAM' package to solve the Navier-Stokes equations and resolve all gradients in a lubricated rolling-sliding contact. The method fully accounts for fluid-solid interactions and is stable over a wide range of contact conditions, including pressures representative of practical rolling bearing and gear applications. The elastic deformation of the solid, fluid cavitation and compressibility, as well as thermal effects are accounted for. Results are presented for rolling-sliding line contacts of an elastic cylinder on a rigid flat to validate the model predictions, illustrate its capabilities, and identify some example conditions under which the traditional Reynolds-based predictions deviate from the full CFD solution.

1. Introduction

Elasto-hydrodynamic lubrication (EHL) is a lubrication regime where a thin lubricant film is formed between two contacting surfaces in relative motion under pressures significant enough to cause considerable elastic deformation of the surfaces. EHL usually occurs in non-conformal contacts and many machine elements, including rolling bearings and gears, rely on EHL in their operation. Although existence of a fluid film sufficient to separate two surfaces under hydrodynamic-rigid conditions, such as in a journal bearing, was known since the work of Tower [1] in 1883, it was not until 1949 [2] that scientists predicted that a thin fluid film can also separate surfaces in high pressure, non-conformal contacts. Clear experimental observation of the EHL film was finally provided by Gohar and Cameron in 1963 [3]. Formation of such a film is possible due to high pressure having two beneficial effects: firstly, it increases lubricant viscosity in the contact inlet and secondly, it elastically flattens the contacting surfaces, hence the term elasto-hydrodynamic lubrication. Classical solutions of elastohydrodynamic contact problems use the Reynolds' equation [4] to describe the behaviour of lubricant in high-pressure, non-conforming contacts, while elastic deformation is usually calculated using Hertz theory of elastic contact. Reynolds's equation is a simplification of full Navier-Stokes equations, derived by assuming a Newtonian lubricant with constant density and constant pressure and viscosity across the film thickness. Cameron et al. [5] and Sassenfeld et al. [6] developed the first Reynolds-based computerised numerical solutions for hydrodynamic lubrication and in 1959 Dowson and Higginson [7] produced the first full numerical solution for EHL. Subsequently, Dowson and co-workers, amongst others, also proposed regression equations for prediction of EHL film thickness based on their numerical solutions [8,9]. These, and similar, EHL regression equations have since found a wide-spread use in tribology. Since then, several studies have shown that, for low sliding speeds and/or loads, physically acceptable results can be obtained with Reynolds assumptions. However, the range of operating speeds and contact pressures in many applications, including rolling bearings, result in shear stresses that generally exceed the limits of Newtonian behaviour for most lubricating oils. Johnson and Tevaarwerk [10], amongst others, showed that the Newtonian model can grossly overestimate the contact shear-stress. Many authors have considered the effects of non-Newtonian behaviour on EHL notably, Najji et al. [11] who derived a generalised Reynolds equation for non-Newtonian flow that can accommodate appropriate rheological models for incompressible fluid and steady-state flow; and Conry et al. [12] who derived a modified-Reynolds equation based on the non-Newtonian rheological model of Eyring.

Schäfer et al. [13] and Bair et al. [14] noted that appropriateness of applying the Reynolds equation to EHL problems is questionable at high pressures (Hertzian) and in high shear-stress regions of the

* Corresponding author.
E-mail address: a.kadiric@imperial.ac.uk (A. Kadiric).

http://dx.doi.org/10.1016/j.triboint.2016.12.046
Received 6 October 2015; Received in revised form 25 December 2016; Accepted 28 December 2016
Available online 29 December 2016
0301-679X/

Nomenclature

α	Pressure viscosity coefficient, 1/Pa
$\alpha_{T,s}$	Thermal diffusivity of solid at temperature T, m^2/s
β	Thermo-viscous constant for a fluid, 1/K
Δt	Time step, s
Δh_d	Rigid displacement increment, m
γ	Diffusion field
$\dot{\gamma}$	Shear rate, 1/s
η	Dynamic viscosity, Pa s
η_p	Low shear-rate dynamic viscosity at pressure p, Pa s
η_0	Dynamic viscosity at atmospheric pressure, Pa s
μ	Kinematic viscosity, m^2/s
μ_s, λ_s	Lame's constants, Pa
υ	Poisson's ratio
ρ	Density, kg/m^3
σ	Stress, Pa
ε	Strain
τ	Shear stress, Pa
τ_0	Eyring stress, Pa
ν	Solid body displacement vector m
A_d	A diagonally dominant and symmetric matrix
E	Young's modulus, Pa
E_r	Reduced Young's modulus $\left(=\pi\left(\frac{1-\upsilon_1^2}{E_1}+\frac{1-\upsilon_2^2}{E_2}\right)^{-1}\right)$, Pa
I	Unit matrix
l	Distance, m
f_b	Body force, N
$P_{r,0}$	Roelands reference pressure, Pa
R	Radius of the contacting cylinder, m
t	Time, s
u	Velocity, m/s
U_e	Entrainment velocity [$=0.5(u_1+u_2)$], m/s
T	Temperature, K
T_0	Ambient temperature, K
V_p	Volume of a control volume (CV) centred on point P, m^3
Z	A constant in Roelands viscosity equation
k	Thermal conductivity, W/(mK)
a_N, a_P	Matrix coefficients
a_s	Sonic velocity in solid, m/s
x, z	Spatial coordinates, m
C_p	Heat capacity, J/(kg K)
$C_{s,v}$	Heat capacity of solid, J/(kg K)
L	Load, N/m
S	Surface area vector

Subscripts

1, 2	identify body 1 and body 2 respectively
l, s, v	identify liquid, solid and vapour respectively

contact. The noted inaccuracies arise due to the assumptions made in derivation of the Reynolds and modified Reynolds equations. Specifically, the gradients of velocity, viscosity and pressure along the film thickness are either significantly simplified or completely neglected. An alternative approach that considers the continuity and momentum equations, which fundamentally describe the fluid dynamics, to fully resolve these gradients can overcome these deficiencies. Such an approach can be achieved through an implementation of a CFD method for EHL problems. CFD offers a number of other benefits over the Reynolds-based models: It considers the entire fluid and solid domains, whereas the Reynolds-based models are limited to the near-parallel contact region; It offers a more accurate treatment for cavitation and greater flexibility in implementing the relationship between fluid properties and pressure, temperature, shear-rate and other contact variables. The only disadvantage of a CFD based method is the considerably lower efficiency in terms of computational cost due to the enlargement of domain size and problem complexity.

Tucker, Keogh and co-workers [15,16] applied CFD techniques to model hydrodynamics of a journal bearing by accounting for thermal and viscous effects. Almqvist and Larsson [17] successfully solved an EHL problem using a commercial CFD-code. They used the Dowson-Higginson expression [18] to model cavitation, the lubricant was assumed to be Newtonian and the Boussinesq solution was used for the elastic deformation. They found good agreement with the Reynolds theory but they did not discuss thermal effects. Subsequently, Almqvist et al. [19] modelled an EHL contact with idealised surface roughness by introducing a single cosine wave (ridge) propagating along contact for pressures of up to 0.6 GPa. This study largely focused on the effect of surface roughness on the pressure distribution.

Hartinger et al. [20] modelled EHL using a CFD model that included cavitation and thermal effects and implemented the Eyring model to describe non-Newtonian fluid behaviour, while the elastic deflection was approximated using Hertzian contact theory. Thermal effects were shown to reduce friction force by up to 88.5% compared to an isothermal solution. Maximum pressure in this model was limited to 0.8 GPa.

Bruyere et al. [21] used a Finite Element method to solve Navier-Stokes equations coupled with elastic deformation. They employed a non-Newtonian rheology model along with compressibility and thermal effects. The cavitation model was simplified using an equation of state limited to the continuity of density-pressure-temperature law over the exit area. Energy equation was assumed to be dominated by high compression and viscous heating. The presented results were in good agreement with the Reynolds and Hartinger et al. models but are limited to a relatively narrow range of contact conditions with pressures of up to 0.7 GPa.

This paper describes a new finite-volume (FV), two-way coupled, solid-fluid solver with reasonable efficiency and computational cost, benefiting from multigrid acceleration and advanced numerical controllers, applicable to both steady-state and transient problems. The advantage of using a single numerical tool enables an internal transfer of information at the fluid-solid interface through a single, common data structure. The present model considers contact conditions pertinent to roller bearings. First, Navier-Stokes equations are solved to provide a fluid solution, which accurately describes the lubricant flow within the contact and the surrounding domain. The considered fluid rheology includes non-Newtonian behaviour and shear-thinning. The phenomenon of cavitation is modelled by implementing a homogenous equilibrium cavitation model, which maintains a specified lubricant saturation pressure in the cavitating region. The current approach solves the full momentum and energy equations, and satisfies continuity. Furthermore, a finite volume solid solver is coupled with the fluid solver in a forward iterative manner to take into account elastic deflection effects resulting in a partitioned two-way-strongly-coupled fluid-solid-interaction (FSI) algorithm. The governing equations and their numerical solutions are implemented using OpenFOAM, a freely available open-source CFD package based on the FV method [22–24]. Current implementation of the model is applicable to two-dimensional, line contacts only, but the general CFD methodology presented is adaptable to three-dimensional problems of elliptical contacts, provided adequate mesh modifications are implemented.

The model offers great flexibility with arbitrarily unstructured 3-D mesh, and accommodation of complex fluid and solid laws is straightforward. The developed method has been applied to a series of

lubricated metal-on-metal line contact problems with slide to roll ratios ranging from 0 to 2 (pure rolling to pure sliding). The results obtained using the new method show a good agreement with Reynolds theory when the fluid is in the Newtonian regime. Thermal and iso-thermal EHL test cases are compared to previously published results to confirm the validity of the model. Further results are presented to show the suitability of the model to study different contact conditions including cases where Reynolds based approaches are unable to provide accurate predictions. Validity of the model over a wide range of EHL conditions and at pressures representative of those found in practical rolling bearing applications is illustrated.

2. Formulation and implementation

The geometry considered by the current model implementation is that shown in Fig. 1 and consists of an elastic half cylinder forming a rolling-sliding, lubricated, line contact with a rigid flat wall. The contact is fully flooded by the chosen lubricating oil and a hydrodynamically generated oil film fully separates the two solid bodies at all times, so that no solid-to-solid contact occurs. The chosen geometry (see Fig. 1) can be considered to simulate a roller – raceway contact in a cylindrical roller bearing provided that the elastic cylinder is assigned a radius, R, equal to the reduced radius of the roller-raceway contact. The cylinder is deformable while the flat is assumed to be rigid. The combined elastic properties of the contacting bodies can be described by the reduced elastic modulus of the contact, E_r. A horizontal velocity is imposed to the raceway (moving wall) while the angular speed of the cylinder is also controlled, so that any slide-roll-ratio (SRR) can be modelled. The chosen coordinate system is such that the origin is in the centre of the cylinder and x and z coordinates are along the rolling-sliding direction and vertically through the film respectively, as shown in Fig. 1.

This section will describe the theory and methodology employed in the current model and its implementation in the OpenFoam CFD package. It should be noted that, although the current implementation of the model is applicable to two-dimensional line contacts only, the presented methodology is easily adapted to a three-dimensional contact by appropriate modifications to the mesh employed. Solution is first presented for the fluid (lubricant) and solid domains, and then the coupling of these two domains through a partitioned, two-way-coupled fluid-solid-interaction (FSI) algorithm is described.

2.1. Fluid solver

The general governing equations for the fluid domain are the continuity and the momentum equations:

$$\frac{\partial \rho}{\partial t}+\nabla.(\rho u)=0 \tag{1}$$

$$\frac{\partial (\rho u)}{\partial t}+\nabla.(\rho uu)+\nabla.\tau=-\nabla(p) \tag{2}$$

where gravitational effects are neglected and τ is the viscous stress tensor given by:

$$\tau = -\mu(\nabla u + (\nabla u)^T) - \mu\frac{2}{3}I\nabla.\, u \tag{3}$$

For an accurate prediction of lubricant behaviour in an EHL contact, the effects of compressibility, cavitation, temperature and lubricant rheology are incorporated in the model.

2.1.1. Compressibility

An understanding of how the lubricant density varies with pressure is necessary for the numerical solution of EHL contacts. In the early development of Elastohydrodynamic lubrication theory, the iso-thermal Dowson-Higginson [25] equation was generally used to consider the pressure-density relationship:

$$\rho(p)=\rho_0\frac{5.\,9*10^8+1.\,34p}{5.\,9*10^8+p} \tag{4}$$

where ρ_0 is the lubricant density at atmospheric pressure and p is in Pa.

2.1.2. Cavitation

Cavitation is formation and activity of bubbles (or cavities) in a liquid and can be divided into four different types: hydrodynamic, acoustic, optic and particle cavitation. In an EHL contacts, found in rolling bearings, we are only concerned with hydrodynamic cavitation [26].

In the Reynolds based approach, cavitation is commonly modelled by forcing pressure to be greater or equal to zero by modifying the Gauss-Seidel matrix solver; an alternative 'penalty' method, proposed by Wu [27], can also be used. In a CFD approach, any unphysical tampering of pressure causes violation of the continuity equation. The current cavitation model, originally developed by Weller [22,24], is a homogenous equilibrium model where a single set of density and momentum equations for the mixture is solved. The saturation pressure (p_{Sat}) of the liquid is maintained in the cavitating region. The liquid is converted into vapour where the pressure drops below p_{Sat}. If the pressure rises above the cavitating pressure, vapour is converted into liquid. In case there is no liquid to convert, pressure will drop below p_{Sat}.

The derivation of Weller cavitation model equations can be re-written as outlined by Hartinger [28], to which the reader is referred to for the full implementation, to include non-linear and unsteady terms of Eq. (2).

2.1.3. Rheology

For a given change in pressure, the change of lubricant viscosity is much greater than the change in its density. Therefore, research has mainly been directed towards obtaining an accurate evaluation of the rheological behaviour, rather than a better description of the compressibility of lubricants in EHL contacts. Pressure-viscosity behaviour at the highest pressure within the contact is necessary for the calculation of traction; therefore applied piezo-viscous model should be capable of estimating correct values of viscosity at high pressures. Advancements in understanding of rheological behaviour of fluids under high pressure, thin film lubrication conditions have led to inclusion of improved physical descriptions in theoretical analyses [29–32]. The majority of work on modifying the Reynolds equation uses the Roelands piezo-

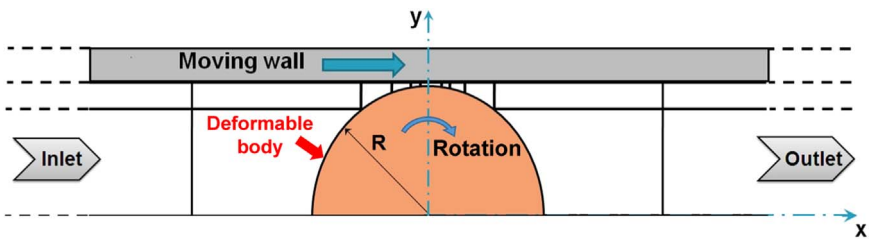

Fig. 1. A schematic illustrating the geometry considered by the present model.

viscous model to account for the effects of pressure and temperature on viscosity [33] through the following equation:

$$\eta_R = \eta_0 \exp\left\{(1n(\eta_0) + 9.67)\left[\left(\left[1 + \frac{p}{p_0}^Z\right] - 1\right)\right]\left(\frac{T - 138}{T_0 - 138}\right)^{-\left(\frac{\beta(T_0-138}{1n(\eta_0)-9.67}\right)}\right\} \quad (5)$$

This was further adapted by Houpert [34] to:

$$\eta_{Roelands-Houpert}=\eta_R \exp\ (-\beta^*(T-T_0)) \quad (6)$$

where Z and β^* are given by:

$$Z=\frac{\alpha}{5.1\times 10^{-9}(\ln(\eta_0)+9.67)}$$

$$\beta^*=[\ln(\eta_0)+9.67][1 + 5.1\times10^{-9}p]^Z\left[\frac{\beta}{\ln(\eta_0)+9.67}\right]$$

where α is the pressure-viscosity coefficient, β is a thermo-viscous constant, η_O is the viscosity at atmospheric pressure, T_O is a reference or ambient temperature and Z is a constant for a given oil independent of temperature and pressure.

Roelands placed an upper pressure limit for the accuracy of his formulation at 0.3–0.5 GPa [33]. However, pressures commonly found in practical concentrated EHL contacts, such as those in rolling bearings, are commonly much higher than these limits. Furthermore, a number of studies have shown that the Roelands' expression is inappropriate even at pressures lower than 0.5 GPa [35,36]. Bair [14] recently carried out a series of experimental investigations at high pressures which suggested that the Yasutomi free-volume model is applicable under EHL contact conditions.

At high loads and high strain rates, there is a large discrepancy between the experimental data and numerical results obtained from Newtonian viscosity models. In order to predict the lubricant viscosity more accurately, thermal and non-Newtonian effects are incorporated in the rheology model.

Sinh-law [37], described by Eq. (7), is commonly used to describe the shear-thinning behaviour of an oil:

$$\dot{\gamma} = \frac{\tau_0}{\eta_p}\sinh\left(\frac{\tau}{\tau_0}\right) \quad (7)$$

Where η_P is the low shear rate Newtonian dynamic viscosity at pressure p and τ_O is a reference stress called the 'Eyring stress', which defines the boundary between Newtonian and non-Newtonian behaviour. If contact shear stress is written as:

$$\tau = \eta_{eyring}\dot{\gamma} \quad (8)$$

then, inserting Eq. (8) into Eq. (7), gives an expression for the shear-thinning viscosity of a fluid:

$$\eta_{eyring} = \frac{\tau_0}{\dot{\gamma}}\sinh^{-1}\left(\frac{\dot{\gamma}\eta_p}{\tau_0}\right) \quad (9)$$

Viscosity η_P needs to account for piezoviscous effects at in-contact pressures, and can be calculated using relationships given in Eqs. (5) and (6) above, so that:

$$\eta_{Eyring-Roelands}=\frac{\tau_0}{\dot{\gamma}}sinh^{-1}\left(\frac{\eta_{Roelands-Houpert}}{\tau_0}\dot{\gamma}\right) \quad (10)$$

At low shear-rate, the resulting viscosity model is equivalent to the implementation of the Roelands viscosity model.

2.1.4. Energy equation

In an EHL contact, heat generated through the relative motion of solid bodies and shearing of the lubricant can significantly change the film behaviour [8–10]. Dowson [29] solved the energy equation, for the first time, in fluid region by assuming that the velocity across the film thickness, and the velocity and temperature gradients along the flow direction, are negligible. Thermal studies of EHL contacts are presented in the pioneering works of Cheng and co-workers [38,39] and Zhu and Wen [40]. Kim and Sadeghi [41] developed an EHL numerical solution for a rolling/sliding point contact in the presence of Newtonian, thermal compressible fluids where the Reynolds, elasticity and energy equations were solved simultaneously with multilevel multigrid techniques. It was concluded that temperature increase in the contact is large and cannot be neglected. Wang et al. [42] developed a computational algorithm to solve non-Newtonian thermal EHL for line contacts. Two different energy equations were implemented to describe the inlet and the back-flow regions [43,44]. They found that thermal effects tend to change the height of the EHL pressure spike as well as its shape. Yang [45] developed a general numerical approach for transient Newtonian thermal EHL for general elliptical point contacts. They provide a comparison between thermal and iso-thermal solutions which indicates that the temperature in EHL contacts can rise by up to 200 °C, and thinner film thicknesses can be predicted relative to isothermal solutions. Habchi et al. [46,47] proposed a finite element model for thermal EHL contacts lubricated with Newtonian and non-Newtonian lubricants, results of which showed that the inclusion of non-Newtonian and thermal effects leads to thinner films at high sliding speeds.

The solution of energy equation is implemented in the present model through the procedure introduced in [20] and will not be repeated here for the sake of brevity. The reader is referred to that reference for further detail.

2.2. Solution for the solid domain

Most EHL simulations involve a combination of finite volume (FV) or finite difference (FD) solver for the fluid and a finite element (FE) solver for the solid. The current model presents a new approach where the FV technique is used for solutions of both the fluid and the solid domain in general EHL problems.

The current implementation of the model assumes that all elastic deformation is accommodated by the half-cylinder while the other surface is assumed rigid.

2.2.1. Deformation

The solid solver incorporates the linear elastic equation (moderate stresses and strains) using an iterative segregated approach and a Langrangian formulation. However, more complex laws can be easily implemented to describe the solid behaviour. The numerical implementation in OpenFOAM is similar to the linear structural solver presented by Jasak and Weller [48].

The force balance of a solid element reads:

$$\frac{\partial^2(\rho_s v)}{\partial t^2} - \nabla.\ \sigma = \rho_s f_b \quad (11)$$

where v is the displacement vector, ρ_s is the solid density, f_b is the body force and σ is the stress tensor.

The plane strain assumption is applied since line contact cases are studied in this paper. The strain tensor is defined in terms of displacements, v:

$$\varepsilon=\frac{1}{2}(\nabla v+\nabla v^T) \quad (12)$$

The stress and strain tensor relation closes the system of equations (Hooke's law):

$$\sigma=2\mu_s\varepsilon+\lambda_s tr(\varepsilon)I \quad (13)$$

where I is the unit tensor and μ_s and λ_s are Lame's coefficients, which are related to Young's modulus of elasticity E and Poisson's ratio υ through:

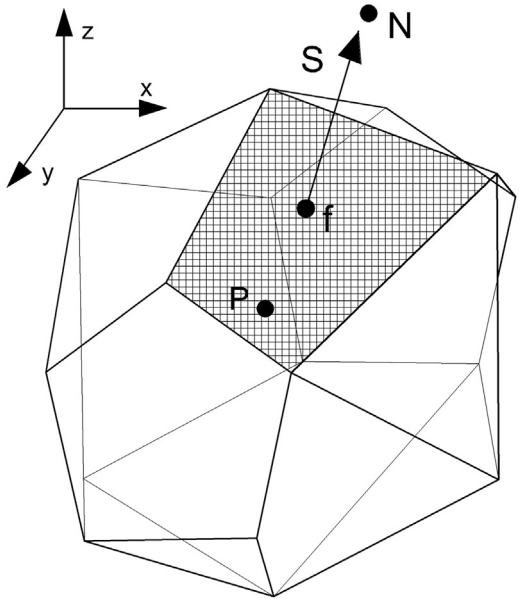

Fig. 2. Schematic of a control volume.

$$\mu_s = \frac{E}{2(1+\upsilon)} \tag{14}$$

$$\lambda_s = \frac{\upsilon E}{(1+\upsilon)(1-2\upsilon)} \tag{15}$$

Eq. (11) can be re-written as:

$$\frac{\partial^2(\rho_s v)}{\partial t^2} - \nabla.\,[\mu_s \nabla v + \mu_s (\nabla v)^T + (\lambda_s Itr\,(\nabla v))] = \rho_s f_b \tag{16}$$

Centroids of two neighbouring control volumes (CV) are shown in Fig. 2, as points P and N; the internal face f is shared only between two CVs and S is the surface area vector.

The equations are discretised in the integral form over the CV and solved in a segregated manner, where each component of the displacement vector is solved separately and the inter-component coupling is treated explicitly. Segregation enables partial convergence and memory use optimisation through solving three smaller matrices consecutively, rather than a large matrix consisting of all three components of displacement. The convergence is achieved when the residuals of all equations drop below a prescribed level.

In order to perform FVM discretisation, Gauss's theorem is applied to the integrated form of Eq. (16) over the CV associated to point P and characterised by volume V_P:

$$\int_{V_P} \frac{\partial^2(\rho_s v)}{\partial t^2} dV = \oint_{\partial V_P} ds.\,[\mu_s \nabla v + \mu_s (\nabla v)^T + \lambda_s Itr\,(\nabla v)] + \int_{V_P} \rho_s f_b\, dV \tag{17}$$

Where $\oint_{\partial V_P} ds$ denotes the surface integral over the CV with volume V_P. The resulting matrices are sparse, diagonally dominant, and the system of algebraic equations on a single cell is given by:

$$a_P v_P + \sum_N a_N v_N = b_P \tag{18}$$

where a_P is a diagonal coefficient that includes contributions from the transient and diffusive terms, a_N is an off-diagonal coefficient generated by the diffusion term, and b_P is the right-hand side coefficient that depends on v values from the previous time step and the previous iteration. Since v_P depends on the values of the neighbouring cell, Eq. (18) can be written as a system of algebraic equations:

$$[A_d][v] = [r] \tag{19}$$

where A_d is the sparse matrix (diagonally dominant and symmetric) with coefficients a_P on the diagonal and coefficients a_N off the diagonal, $[v]$ is a vector consisting of displacement increments for all the CVs and $[r]$ is the right hand side vector consisting of source terms for all CVs. The system of equations is solved by using a segregated algorithm, where three components of displacement vector increment are solved separately from each other. The matrix A_d is symmetric and diagonally dominant and is solved with a conjugate gradient Cholesky preconditioned solver [23,49] which provides accuracy and computational time efficiency.

2.2.2. Energy equation

The energy conservation for a solid cell can be written as:

$$\rho_s C_{s,v} \frac{\partial T}{\partial t} = \nabla.\,(k_s \nabla T) + -\rho_s C_{s,v} \dot{v}.\,\nabla T + \frac{\partial k_s}{\partial T} (\nabla.\,\mathrm{T})^2 \tag{20}$$

where $\dot{v}$ is the velocity of solid cell. For the presented cases in this paper, the solid thermal conductivity is assumed to be constant and therefore the last term on the right hand side of Eq. (20) is neglected. The Laplacian term (the first term on the right hand side of Eq. (20)) is discretised using Gauss linear corrected scheme, the divergence term is discretised using Gauss linear scheme, the gradient terms are calculated based on Gauss linear discretisation and finally, the Euler implicit scheme is used for the discretisation of the time derivatives [49].

2.2.3. Load balance

To check for load convergence, the pressure distribution force is evaluated numerically at the end of each time step to compare the current load, L, carried by the EHL film, with the target load L_{aim}. The current load is calculated through the integral form of pressure distribution acting on the deformed surface.

A characteristic deformation time, t_d, is defined to introduce a dependency on time-step Δt:

$$t_d = \frac{R}{a_s} \tag{21}$$

where R is the radius of the contacting cylinder and a_s the sonic velocity in the solid material (taken as 5000 m/s). The final rigid displacement increment prescribed at the remote boundaries of the solid body to achieve the prescribed load is given by:

$$\Delta h_d = (v_{max} - v_{min}) \frac{L_{aim} - L}{L_{aim}} \frac{\Delta t}{t_d} r_d \tag{22}$$

where v_{max} and v_{min} are the maximum and minimum deflections in the solid domain and r_d is the under-relaxation factor for deflection. For stability reasons, Δh_d is limited by the prescribed maximum velocity of the solid body of 2.10^{-3} m/s.

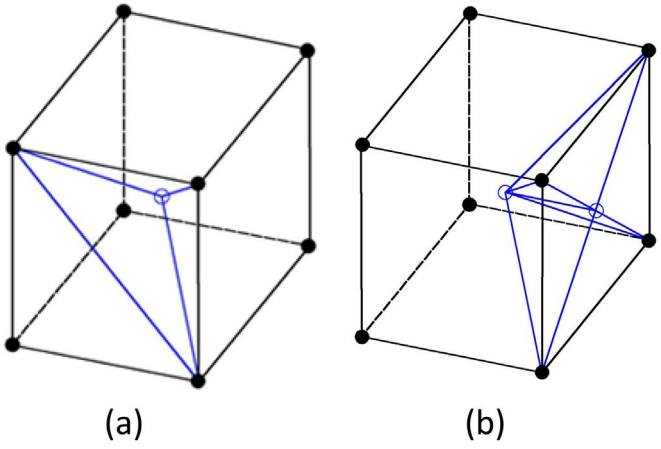

Fig. 3. Decomposition of a polyhedral cell into tetrahedral elements.

2.3. Fluid solid interaction

An FSI model is used to describe a dynamic system influenced by the interaction of a moving fluid and a deforming solid. Therefore, a major aspect of FSI analysis is the coupling of the fluid and solid domains, which manifests itself in both the mesh movement linked to the elastic deflections and the heat generation and transfer between the fluid and the solid domain.

2.3.1. Moving mesh

Dynamic mesh deformation models using FV techniques are limited to spring analogy and triangular cells. These methods are proven to be weak particularly for arbitrarily unstructured meshes that are common in FV simulations [50]. Dynamic mesh motion is instead adopted in the current model in a similar manner to the FV dynamic mesh motion proposed by Jasak and Tukovic [51].

The current method is devised for arbitrary polyhedral mesh composition. Polyhedral cell is split into tetrahedrals by splitting its faces into triangles and introducing a point at the cell centroid (Fig. 3a). Identical face decomposition is used for both cells sharing an internal face (Fig. 3b).

Laplacian operator is well suited for mesh motion solver as it is always bounded. Moreover, the use of tetrahedral elements, for a Laplacian operator, produces a diagonally dominant matrix that increases computational efficiency. The Laplacian operator with distance based diffusion field (γ) is chosen to govern mesh motion.

$$\nabla.(\gamma\nabla u)=0 \tag{23}$$

where u is the point velocity field used to modify point positions:

$$x_{new}=x_{old}+u\Delta t \tag{24}$$

where x_{old} and x_{new} are the point positions before and after mesh motion. The mesh updates according to displacement increment.

A linear distance based method is implemented where the diffusion field γ is a function of cell centre distance, l, to the nearest prescribed boundary patches.

$$\gamma=\frac{1}{l} \tag{25}$$

Eq. (24) is discretised over the tetrahedral decomposition using a second-order accurate method. The produced matrix is solved with an iterative linear equation solver using the Incomplete Cholesky preconditioned Conjugate Gradient (ICCG) algorithm [49].

2.3.2. Heat transfer

A multi-region coupling strategy is implemented for thermal modelling of fluid-solid interaction. By the use of a similar decomposition method, both meshes decompose at the same coordinate location. The fluid temperature equation is solved subject to the appropriate Drichlet boundary condition ($T_f=T_s$) at the coupled interface (see Fig. 4). Subsequently, the solid temperature equation is solved subject to Neumann boundary condition $q_s^{"}=q_f^{"}$ at the coupled interface. These two steps are repeated until final convergence is achieved.

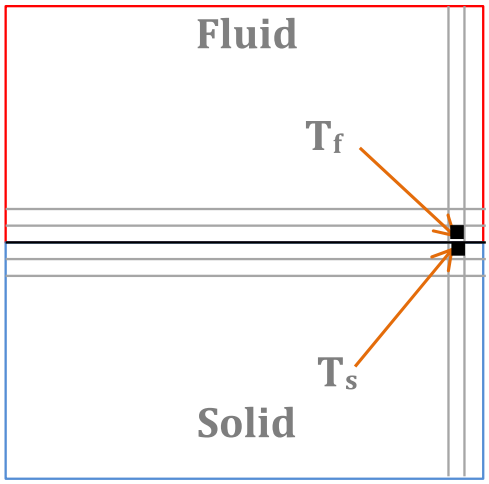

Fig. 4. Interfacial cells in solid and fluid domains.

2.3.3. FSI solver algorithm

Fluid-solid interaction solvers can generally be divided into monolithic (or implicit) and partitioned (or explicit) where separate solutions for fluid and solid domains are obtained and some kind of iteration scheme is used to account for interactions at the fluid-solid boundary [52]. The partitioned solvers can be further divided into one-way coupled, where only the influence of fluid forces on the solid deformations are considered, and two-way coupled, where the influence of the resulting solid deformations on the fluid domain is also considered. Finally, two-way-coupled partitioned methods can be divided into weakly-coupled, where no convergence at the fluid-solid boundary is sought at each time step, and strongly-coupled, where convergence at solid-fluid boundary is achieved at each time step [52]. Using these definitions, the FSI algorithm implemented in this paper is best described as partitioned, two-way-strongly-coupled solver i.e. both the influence of fluid forces on the solid and the resulting solid deformations on the fluid are accounted for and sub-iterations are performed to ensure that the fluid and solid interactions are converged at the fluid-solid boundary at each time step.

The initialization of the solver in Reynolds based approach is normally done with dry Hertzian contact solution. However, the current cavitation model becomes unstable if initialised with a prescribed deflection. Instead, solid and fluid bodies in the present model are separated by an initial gap (0.1 μm was found to be numerically stable for the cases analysed here). The bodies are pressed together, using Eq. (22), until the target load is reached. The fluid domain is solved using an algorithm similar to the Pressure-Implicit Split-Operator (PISO) [23,49]. The general procedure of the fluid-solid structure solver is illustrated in Fig. 5. All fluid governing equations, continuity, temperature and pressure equations are solved using GAMG matrix solver, while the solid governing equations are solved using the Cholesky preconditioned conjugate gradient solver [23,49].

3. Results and discussion

The geometry considered in all case studies in this section is that shown in Fig. 1. The half-cylinder is assigned elastic material properties while the wall is considered rigid so that the combined material properties of the contacting bodies are described by a reduced elastic modulus, E_r $\left(=\left(=\pi\left(\frac{1-\upsilon_1^2}{E_1}+\frac{1-\upsilon_2^2}{E_2}\right)^{-1}\right)\right)$. All common case parameters used throughout the paper are listed in Tables 1–3. Table 1 lists the general parameters while thermal properties of the lubricant and the solid are listed in Tables 2 and 3 respectively. The remaining, case specific parameters, including the entrainment speed, slide-roll-ratio, load and lubricant viscosity, are listed in each figure caption corresponding to the case being considered.

The boundary conditions for density are zero gradient at all boundaries. The pressure gradient is zero at the walls and pressure is fixed to ambient pressure at inlet and outlet. The boundary conditions for velocity are set in accordance with the imposed slide-to-roll ratio and velocity directions are as shown in Fig. 1. The velocity at the inlet and outlet is calculated according to the mass-flux.

The chosen basic geometry of a cylinder on flat is intended to simulate a roller-raceway contact in a cylindrical roller bearing. Of course, an actual roller bearing encompasses a series of cylinder-raceway contacts and therefore periodic boundary conditions may be

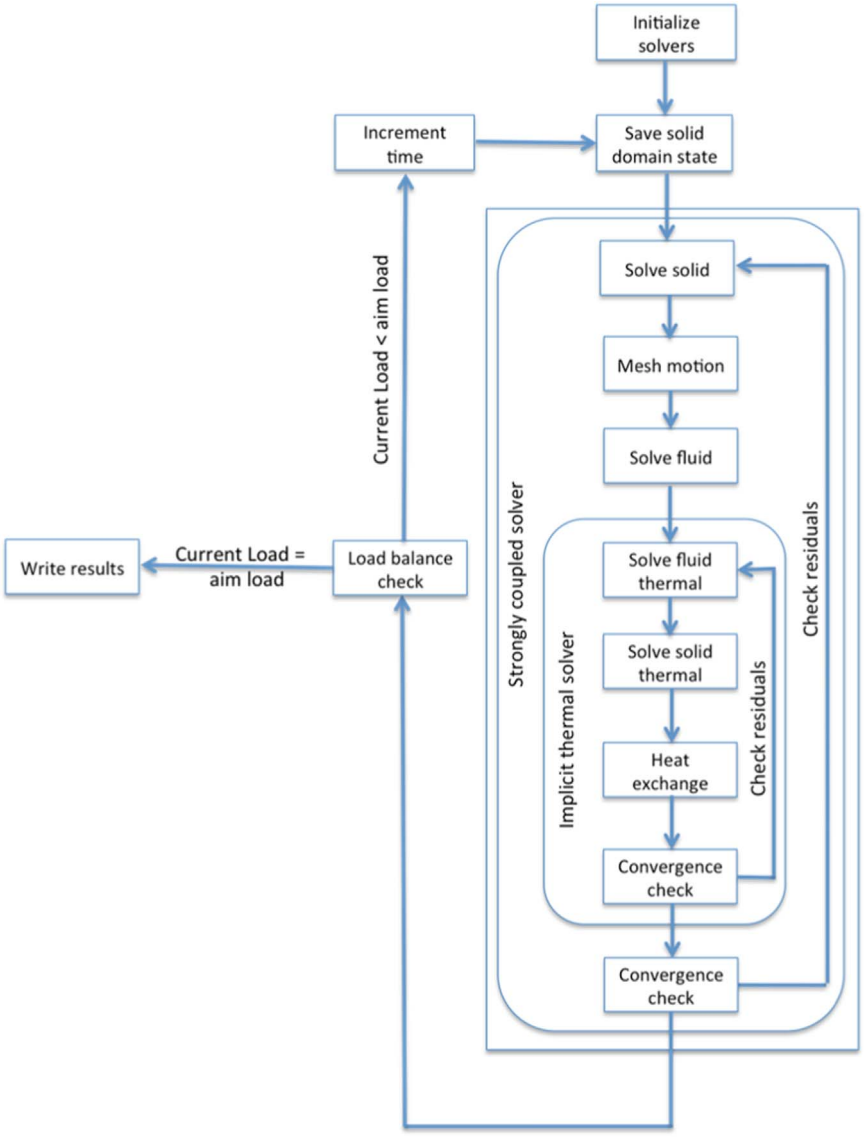

Fig. 5. A flow chart of the complete model algorithm.

Table 1
EHL case parameters.

Parameter value	
Cylinder radius	R=0 mm
Domain length	L=120 mm
Initial minimum gap	h_i =0.1 μm
Thermo-viscous constant	B=0.0476 1/K
Roelands reference pressure	$P_{r,O}$=1.98. 10^8 Pa
Liquid density at p_{vapour}	$\rho_{l,\ sat}$=850 kg/m^3
Roelands pressure index	z=0.689
Eyring stress	τ_O=5.0 MPa
Ambient pressure	p_O=10^5 Pa
Ambient temperature	T_O=353 K
Vapour pressure	p_{vapour}=5000 Pa
Vapour density at p_{vapour}	$\rho_{v,\ sat}$=0.0288 kg/m^3
Dynamic viscosity vapour	μ_l=8.97×10^{-6} m^2/s

considered to be physically more acceptable. Consequently, additional cases with periodic boundary conditions at the inlet and the outlet have also been tested to ensure the validity of the chosen boundary conditions. These tests have shown that the boundary conditions outlined above are representative for the configuration considered.

The convergence criterion for each parameter is set separately and iteration is only stopped once all residuals are below their respective convergence criteria (pressure and velocity 10^{-12}, temperature and density 10^{-10} and deformation 10^{-9}). To improve stability, the deflection under-relaxation factor is set to values in the range 0.01–0.05, depending on speed and pressure ranges. The time step value is varied between 10^{-10} and 10^{-8} s, depending on the particular conditions of the case studied. It should be noted that it is possible to partition the solution domain into sub-domains, in which case different time steps may be used in different parts of the domain in order to reduce the computation time. The number of inner correctors for the solid deformation loop is related to the range of pressure values.

3.1. Model validation

3.1.1. Mesh convergence and stability considerations

The computational domain studied in this paper is shown in Fig. 6. The figure attempts to illustrate the complexity of the mesh generation for the fluid domain, which arises due to the very low value of film thickness with respect to the fluid domain to be simulated, and schematically describes the strategy followed by the authors to discretise the fluid domain.

Table 2
Thermal properties of the lubricant.

Parameter value	
Specific heat capacity liquid	$C_{p,l}$ =2300 J/(kg K)
Specific heat capacity vapour	$C_{p,v}$ =1800 J/(kg K)
Thermal conductivity liquid	k_l=0.15 W/(m K)
Thermal conductivity vapour	k_v=0.025 W/(m K)
Heat of evaporation	h_{evap}=287 kJ/kg

Table 3
Thermal properties of the solid cylinder (typical bearing steel).

Parameter value	
Density solid	ρ_s=7850 kg/m^3
Specific heat capacity solid	$C_{v,s}$=450 J/(kg K)
Thermal conductivity solid	k_s=47 W/(mK)
Thermal diffusivity solid	$\alpha_{T,s}$= 1.31×10−5 m^2/s

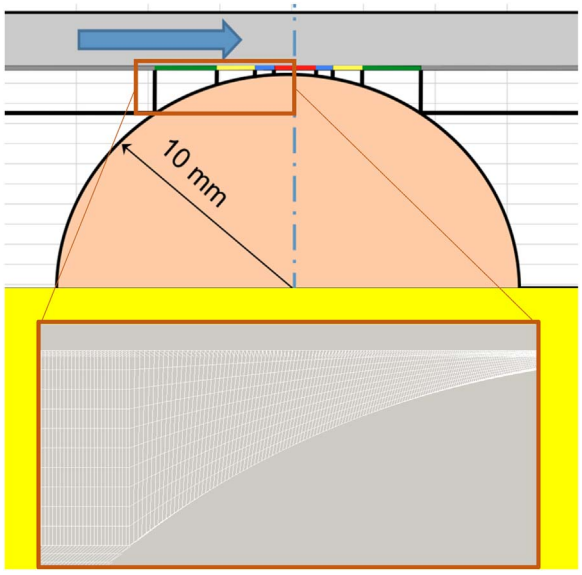

Fig. 6. Subdivision of the computational domain and fluid mesh discretisation (inset). (For interpretation of the references to color in this figure legend, the reader is referred to the web version of this article.)

Table 4
Details of mesh convergence study reporting the maximum relative % error in pressure, with respect to the Reynolds equation solution for the equivalent case, for a varying number of mesh nodes in the fluid domain (pure sliding case with a Newtonian fluid).

Total number of nodes in the fluid domain		X			
		874	1748	**3496**	6992
Z	2	1.813	2.145	2.463	2.601
	5	0.983	0.426	0.447	0.521
	10	1.361	0.296	**0.112**	0.121
	20	1.781	0.312	0.106	0.109

Table 5
CFD isoviscous-incompressible case parameters used in mesh convergence study.

Parameter	Value
Cylinder radius	R=10 mm
Moving wall velocity	u=1 m/s
Film thickness	h_0=10^{-7} m
Viscosity	η=0.04201 Pa s

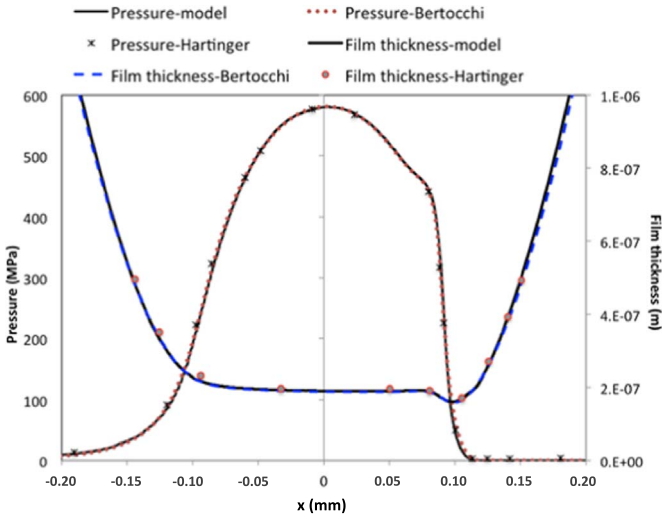

Fig. 7. Film thickness and pressure distributions for an isothermal case (U_e=2.5 m/s, E_r=345.23 GPa, SRR=2, L=10^5 N/m, η_0=0.01 *Pa s*) as predicted by the current model compared with the equivalent results from Hartinger et al. [20] and Bertocchi et al. [53].

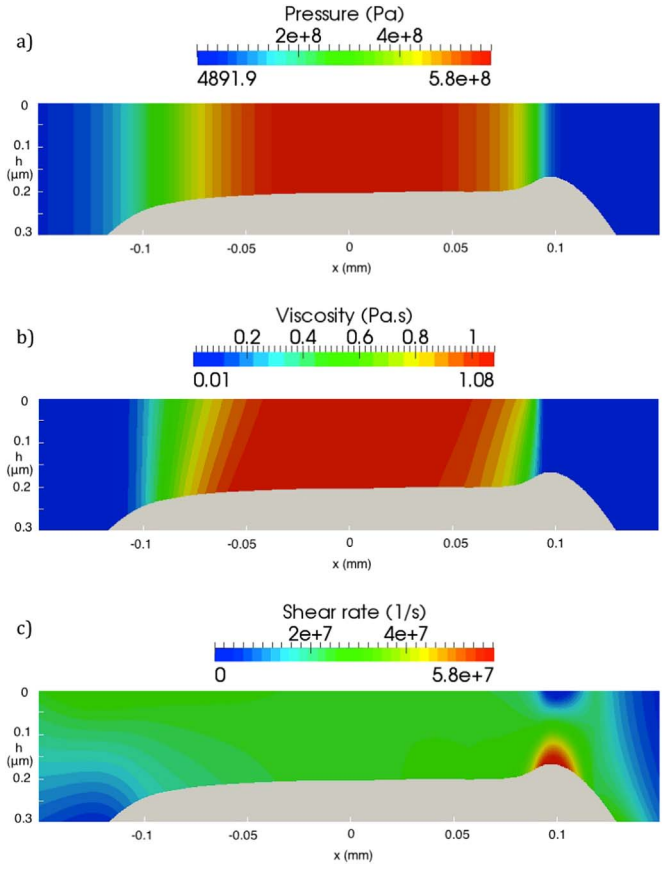

Fig. 8. (a) Pressure, (b) Viscosity and (c) Shear rate distributions for the same case as shown in Fig. 7 above (Isothermal solution, U_e=2.5 m/s, E_r=345.23 GPa, SRR=2, L=10^5 N/m, η_0=0.01 *Pa s*,).

For the standard case studied here (R=10 mm), the domain was subdivided into blocks and different expansion ratios were set in different blocks to maintain aspect ratios of less than five between the neighbouring elements. For this purpose, the surface of the moving wall was divided into segments (identified in Fig. 6 by different colours) each of which was assigned a different number of nodes so that the mesh density is the greatest in the central part of the contact region (red segment in Fig. 6) and gradually decreases away from it.

In order to test mesh sensitivity and stability of the code for the fluid solver, a mesh refinement study was carried out by running the model with an increasing number of nodes in the x and y directions, and in each instance comparing its predictions to those obtained with Reynolds equation for the equivalent case. Table 4 shows results of such a study for a case with Newtonian lubricant under pure sliding at 1 m/s. All input parameters for this case are listed in Table 5; the fluid is isoviscous and incompressible, and its viscosity is typical of a lubricant used in rolling bearing applications. Initial tests were performed using the simpleFoam solver, a steady-state solver for incompressible and isoviscous fluids, whose governing equations are continuity and momentum. As for the general solver, the equations were discretised using second-order central differencing. ICCG (incomplete-Cholesky preconditioned conjugate gradient) and BICCG (incomplete-Cholesky preconditioned biconjugate gradient) solvers were used for pressure and velocity matrices respectively [49]. The residual tolerances are set to 10^{-6} for both velocity and pressure.

The finest mesh in the sensitivity study illustrated in Table 4 consists of 139840 cells: 20 elements are uniformly distributed across the fluid film (y direction) while 6992 nodes are employed to discretise the domain in the x direction (the full domain extends 14.14 *mm* and is centred in correspondence to the axis of the cylinder). Coarser meshes were obtained by lowering the number of cells in both directions. A single execution of the main loop for the fluid solver (see Fig. 5) takes 16 s on a single Intel Core i7 3.2 *GHz* processor for the most refined mesh. The maximum % error for each mesh reported in Table 4 indicates that, in this example, a mesh independent solution is achieved with 34960 total nodes (3496 in x and 10 nodes in y direction).

Similar mesh refinement studies were conducted for all cases reported here. The computation was performed using the same multi-block discretised domain. For the most demanding cases, associated with large pressure gradients, it was necessary to use 80,000 cells in the central mesh segment of the fluid domain identified by the red colour in Fig. 6 (4000 nodes in the x direction, and 20 nodes in the y direction) which corresponds to 88,000 cells covering the complete fluid domain.

In the solid domain, the number of cells is dictated by the accuracy required to capture the high pressure thermal cases. In the cases presented here, the nodes along the perimeter of the cylinder are set to match the mesh used in the fluid domain so that the solid mesh is graded radially to decrease the number of elements used away from the contact. However, additional tests were conducted to show that non-conforming meshes, where nodes at the fluid/solid interface are not matched, can also be adopted in combination with appropriate numerical schemes to interpolate values across the interface cells. Solid cells ranged from 44,780 to 154,560 (thermal and isothermal respectively). One execution of the main loop for the fluid-solid solver (see Fig. 5) takes 3 min on a single core Intel i7 3.2 GHz processor with 32 GB RAM for the most extreme cases reported here. As an indication of the order of magnitude of the total computational time required to obtain a fully converged solution, the case illustrated in Figs. 7 and 8 below took approximately 20 days on the same *single* core Intel i7 3.2 GHz processor with 32 GB of RAM.

3.1.2. Isothermal solution

In order to further validate the current model, its predictions are compared with the equivalent results obtained by Hartinger et al. [20] who also used a CFD based finite-volume approach. In addition, the current predictions are also compared to those obtained using the methodology developed by Bertocchi et al. [53] which is based on a mass-conserving formulation of the Reynolds equation proposed by Giacopini et al. [54] and has been modified to include elastic deformations. The first case studied is an iso-thermal pure sliding case ($SRR =$ 2) with entrainment velocity (u_e) of 2.5 m/s. The lubricant is assumed to be non-Newtonian and can undergo shear-thinning with initial dynamic viscosity of η_O=*0.01* (Pa s); the target load being 10^5 N/m.

Fig. 7 shows the comparison of isothermal pressure distribution and film thickness predictions from the current model to those of Hartinger et al. [20] and Bertocchi [53]. A complete agreement is evident in both the film thickness and pressure predictions.

Pressure, viscosity and shear rate distributions for this case are shown in Fig. 8(a), (b) and (c) respectively. Maximum viscosity within the contact reaches 1.08 *Pa s* and some variation of viscosity through the film is evident in the centre of the contact due to shear-thinning. The maximum shear rate is seen to occur at the exit constriction, near the stationary cylinder. The fluid film pressure is constant through the film thickness for this case, characterised by relatively low viscosity. These observations are in line with those predicted by Hartinger [28] for the equivalent case of pure sliding with relatively low viscosity lubricant.

3.1.3. Thermal solution

In order to validate the full model, including thermal effects, the results from a thermal case study are compared with the equivalent thermal results of Hartinger et al. [20]. Fig. 9 compares the pressure and film thickness results for a pure sliding case with η_0=0.01 Pa s obtained with the current model, for a case where both bodies are treated as conductive, with the results of Hartinger et al. [20] for the same conditions. A good agreement between the two models is evident, particularly given the fact that Hartinger et al. data was digitised from a printed plot published in [20] and that their model uses Carslaw and Jaeger solution for the thermal boundary conditions on the moving solid surface (see [20]), whereas the shown solution from the current model fully solves for the heat transfer within the solid bodies.

Fig. 10 shows the viscosity, temperature, shear rate and pressure distributions for the same conditions (SRR=2 and η_0=0.01 Pa s). Results are for a thermal solution but the temperature of the top, moving wall in this case was held constant. The maximum viscosity of 1.81 Pa s, which occurs on the faster moving wall, is higher than the maximum viscosity predicted in the equivalent isothermal solution (1.08 Pa s, Fig. 8(a)). The difference occurs due to the fact that less shear-thinning is occurring when the thermal effects are accounted for. Non-constant lubricant viscosity through the film is predicted due to non-Newtonian and thermal effects. Standard Reynolds solution assumes that the viscosity is constant across the film thickness and is therefore unable to pick up this viscosity gradient through the film. It should be noted that the generalised form of Reynolds equation [12,29] includes differential terms accounting for viscosity variation across the film; however, the full solution of this generalised equation requires the

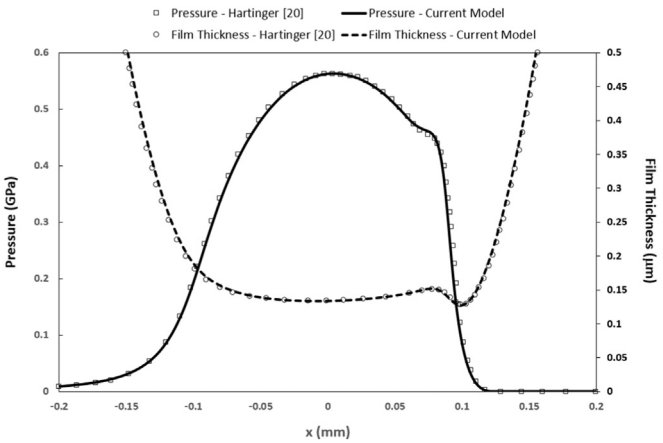

Fig. 9. Film thickness and pressure distributions for a full thermal solution (all bodies conductive) compared with equivalent results of Hartinger et al. which were digitised from the published plot in [20]. (U_e=2.5 m/s, E_r=345.23 GPa, SRR=2, L=10^5 N/m and η_0=0.01 Pa s).

functional relationship between viscosity and distance through the film

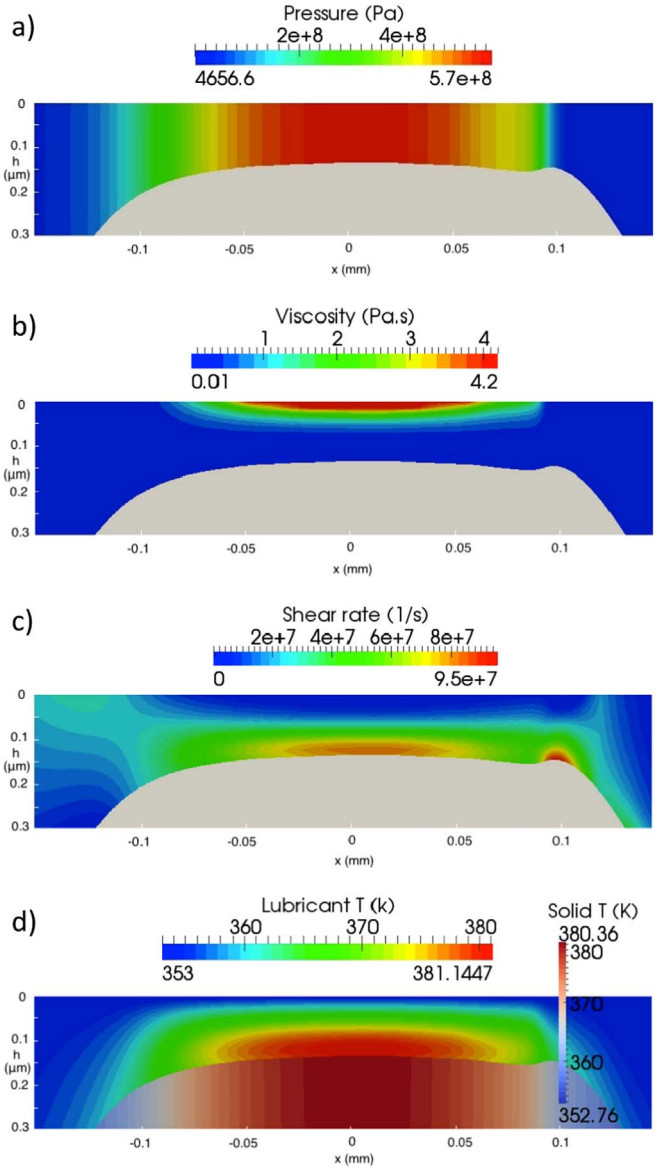

Fig. 10. a) Pressure b) Viscosity c) Shear rate and d) Temperature distributions in fluid and solid (note different colour scales) for the thermal solution (top wall temperature constant) with the same conditions as in Fig. 9i.e. U_e=2.5 m/s, E_r=345.23 GPa, SRR=2, L=10^5 N/m and η_0=0.01 Pa s).

to be known, but since this is usually unknown, approximations are commonly used.

Lubricant temperature rises by up to 27 K in the central region of the contact with the maximum temperature occurring at lower stationary surface. As a consequence of this, the viscosity in this region is lower. Some downstream conduction of heat occurs which results in the lower lubricant viscosity at the inlet. As was observed for the isothermal case of Fig. 8, the maximum shear rate occurs at the stationary surface in the constriction region, while there is no significant variation in pressure through the film. The predicted distributions of viscosity, temperature, shear rate and pressure presented here are again similar to those shown by Hartinger et al. [20] for the same thermal case, with any differences arising from the fact that Hartinger et al. used Carslaw-Jaeger boundary conditions for the

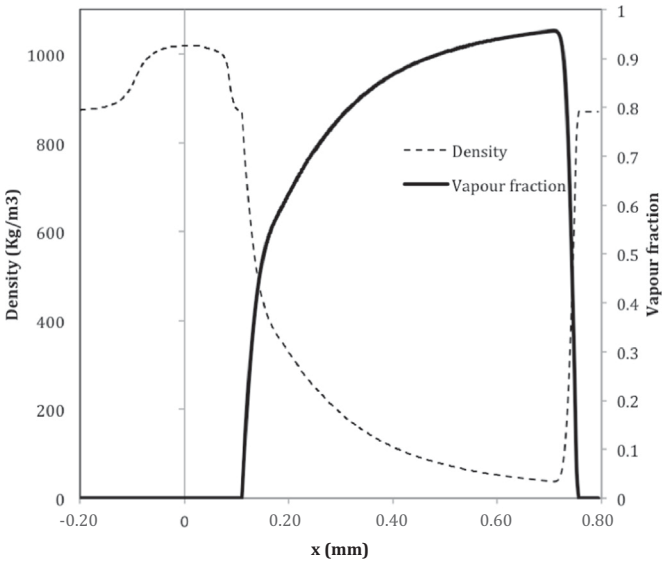

Fig. 11. Density and vapour fraction along the rigid moving wall showing the cavitation and reformation along the contact (isothermal solution, U_e=2.5 m/s, E_r=345.23 GPa, SRR=2, L=10^5 N/m and η_0=0.01 Pa s).

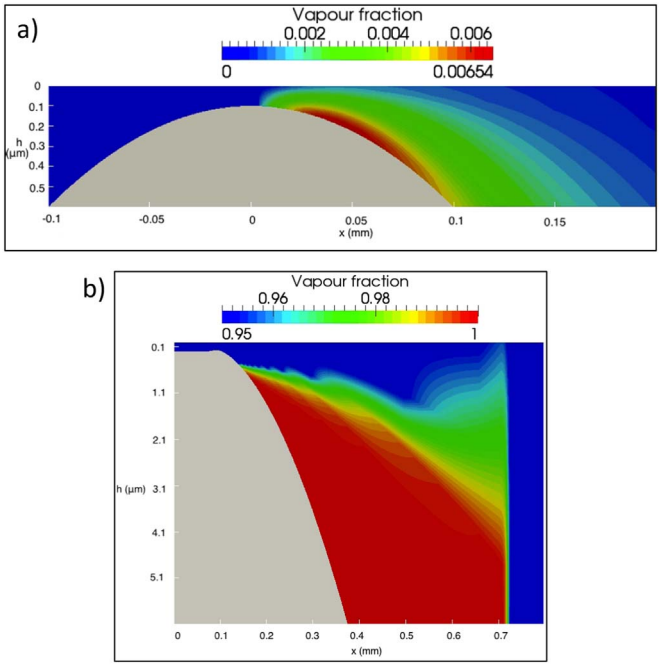

Fig. 12. Vapour fraction distributions for the pure sliding case shown in Figs. 7, 8 and 11 (U_e=2.5 m/s, E_r=345.23 GPa, SRR=2, η_0=0.01 Pa s, L=10^5 N/m); a) t=1.2*10^{-6} s; b) t=0.0002157 s.

moving wall rather than a fixed temperature.

3.2. Cavitation

To illustrate the model capabilities in regards to cavitation, Fig. 11 plots the density and vapour fraction distributions along the rigid wall for the same isothermal solution that was shown above in Figs. 7 and 8. Cavitation formation and reformation are evident in the plot. The cavitating zone starts immediately after the constriction (x=0.1 mm) and ends at x=0.75 mm; the density of lubricant drops to as low as 40 kg/m^3 in the region near the end of the cavitating zone.

Fig. 12 shows the full distribution of vapour fraction for the same case at two different time steps, t=1.2*10^{-6} s illustrating the origina-

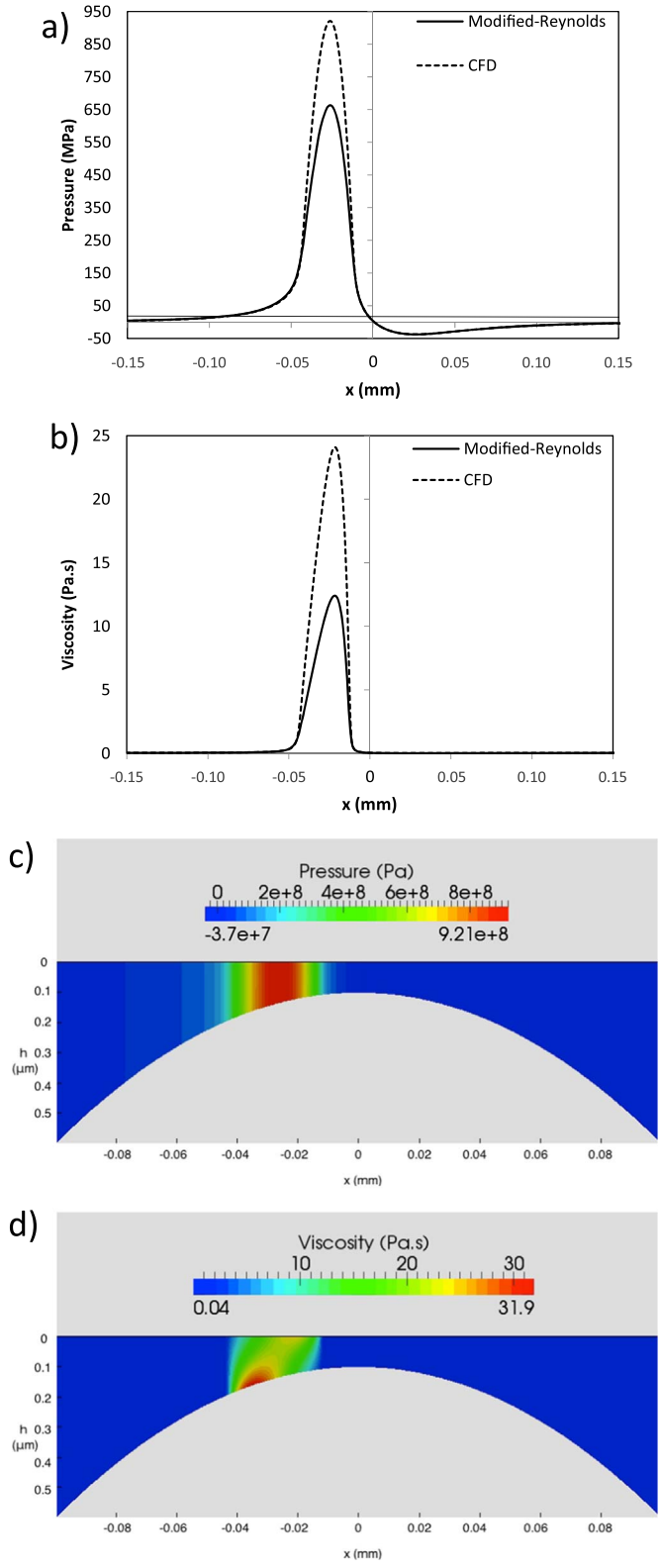

Fig. 13. Comparison of CFD predictions with those obtained with a modified Reynolds solution of Conry et al. [12] for an example case (isothermal solution with pure sliding, rigid solids, non-Newtonian fluid and fixed film thickness). Wall sliding velocity=0.5 m/s, η_0=0.04201 *Pa s*. a) Comparison of pressure predictions; b) Comparison of viscosity solutions; c) Contours of pressure predicted by the CFD model; d) Contours of viscosity predicted by the CFD model.

tion of cavitation, and at t=2.157*10^{-4} s, illustrating the fully cavitated region. As may be expected, cavitation starts at the stationary (or lower speed) surface in the contact, in this case the cylinder, while the moving surface is able to 'drag' the fluid along.

3.3. Comparison between current CFD model predictions and Reynolds solutions

One of the advantages of the current model over standard or modified Reynolds based solutions is its ability to resolve pressure and viscosity gradients through the film thickness and fully account for thermal and non-Newtonian fluid effects. As may be expected, predictions for the two approaches agree well within the Newtonian region but differences become apparent at higher sliding speeds where the lubricant starts to shear thin. To illustrate this, Fig. 13 compares pressure and viscosity predictions of the current model to Reynolds-Eyring model of Conry et al. [12] for an example isothermal, pure sliding case where the wall speed is 0.56 m/s. Given the relatively high sliding speeds, this modified-Reynolds solution is used for comparison instead of the standard Reynolds approach. One of the major shortcomings of Reynolds based approaches is their isothermal assumption, although some authors have recently presented a thermal-Reynolds approach [55]. Present authors do not have access to such a thermal-Reynolds model but since the aim of this section is to illustrate the basic differences between CFD and Reynolds approaches, a like-for-like comparison is ensured by using an isothermal solution with rigid solids in both CFD and modified-Reynolds predictions of Fig. 13. The differences in both pressure and viscosity are evident in Fig. 13a and b. To help explain these differences, Fig. 13c and d show the CFD predictions for pressure and viscosity through the film. Although the pressure is relatively constant through the film thickness, viscosity is seen to vary considerably due to relatively high shear rates. The ability of the CFD model to account for this viscosity gradient in z-direction is an improvement over Reynolds based models and results in the differences evident in Fig. 13a and b.

3.4. CFD Predictions at high pressures

One of the limitations of existing CFD models of EHL contacts is that their numerical stability appear to be limited to a relatively narrow range of contact conditions, and relatively low pressures in particular. For example the maximum Hertz pressure achievable in Hartinger et al. [20] model was 0.8 GPa. This is a serious drawback as the practical EHL contacts to which these models need to be applied commonly operate at much higher pressures, for example in a rolling element bearing pressures in the contacts of the rolling elements and races are commonly 1–2 GPa, and can be as high as 4 GPa. Rather than contact pressure alone, a more useful way of assessing the stability of EHL models is in terms of the range of dimensionless parameters that the model can deal with. Dimensionless parameters commonly used in EHL theory are the speed parameter, $\overline{U} = U_e\eta_0/E'R$, the load parameter, $\overline{W} = L/E'R$, and the material parameter, $\overline{G} = \alpha E'$, where $E' = 2[(1-\upsilon_1^2)/E_1 + (1-\upsilon_2^2)/E_2]^{-1}$ and all other variables are as defined earlier. Using these parameters, the stability of Hartinger et al. [20] CFD model was illustrated for a limited range of material and load parameter values in particular, ($\overline{G} < 7.4.10^3$ and $\overline{W} < 9.10^{-5}$), which translates into relatively low achievable pressures, unrepresentative of practical applications as discussed above. Therefore, in order for the apparently sophisticated CFD models to be useful in practice, they must be capable of dealing with a wider range of conditions and higher contact pressures. The CFD method presented here is stable over a wider range of conditions, including pressures of over 3 GPa. This section presents a selection of cases to illustrate the stability of the model over a wide range of conditions. Wider range of conditions and higher pressures are achieved by increasing the initial dynamic viscosity of the lubricant, assigning a higher elastic modulus to the elastic cylinder (E=400 GPa), and increasing the applied load (up to 600 kN/m in cases below). In all cases, a constant temperature is prescribed to the moving wall while full heat transfer problem is solved

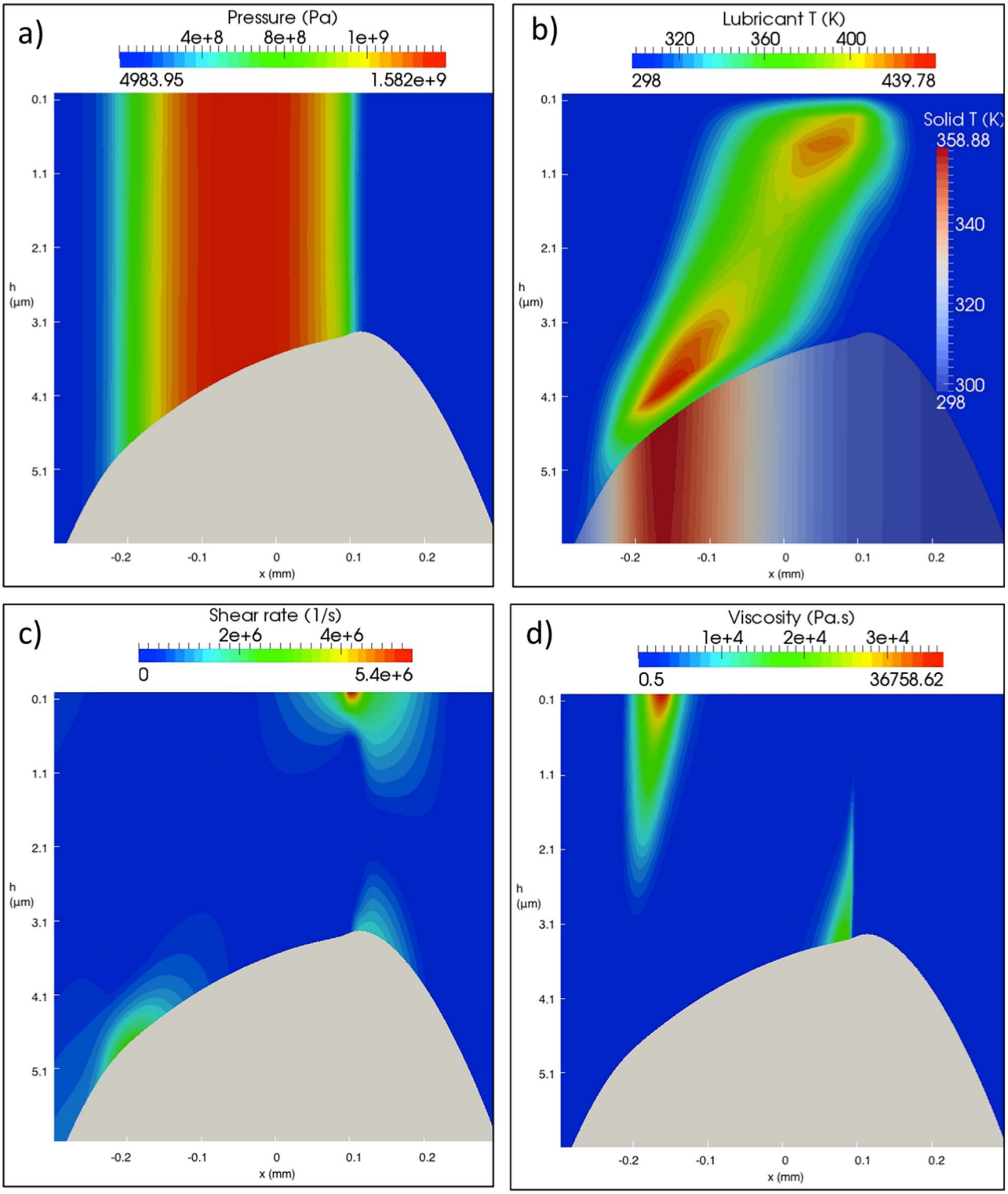

Fig. 14. Thermal solution results for the case U_e=2.5 m/s, SRR=0.4, η_0=0.5 Pa s, E_r=690.46 GPa (i.e. E_{cyl}=200 GPa and rigid wall), Converged load =420 kN/m; (a) Pressure, (b) Temperature, (c) Shear rate, and (d) Viscosity.

in the conductive cylinder.

Fig. 14 shows the results of a thermal solution for the case where SRR=0.4, η_0=0.5 Pa s, E_r=690.46 GPa and the converged normal load is 420 kN/m. The converged pressure reaches as high as 1.6 GPa (Fig. 14a). Lubricant temperature distribution shows two local maxima with the maximum temperature rise being over 140 K (Fig. 14b). This in turn results in lower viscosity values in the same regions (Fig. 14d). The location of the local temperature maxima also coincides with the locations of high shear rate gradients (Fig. 14c). The increased temperature in the central region between the surfaces results in a lower viscosity and consequently leads to the development of a marked shear band. The maximum viscosity of 36758 Pa s occurs at the rigid wall and the local viscosity maxima in the region of the highest pressure gradient are also notable.

An equivalent solution for a pure sliding case is shown in Fig. 15. Maximum pressure in this case is about 1.3 GPa (Fig. 15a). As may be

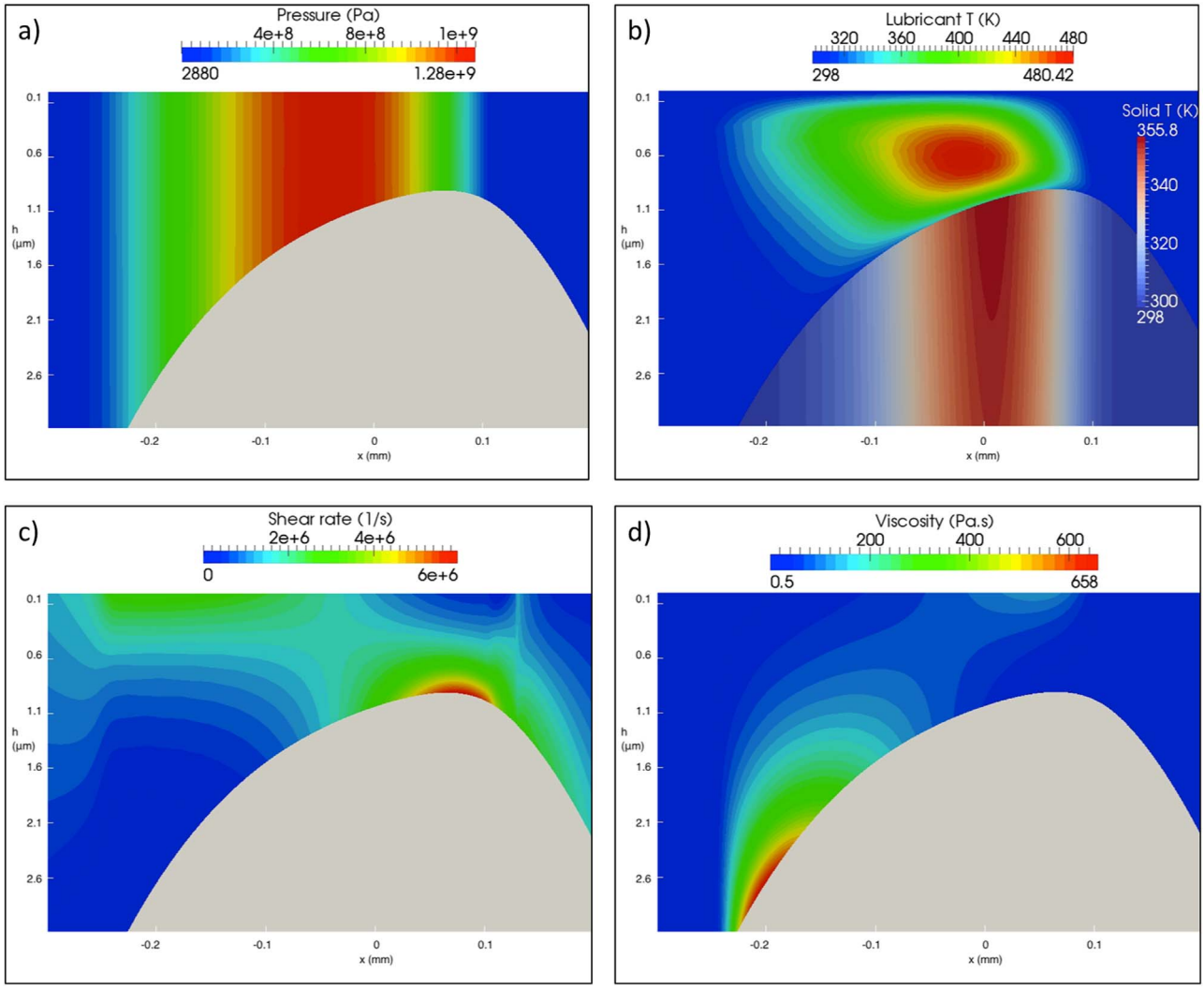

Fig. 15. Thermal solution results for the case U_e=2.5 m/s, SRR=2, η_0=0.5 Pa s, E_r=690.46 GPa, Converged load =400 kN/m; (a) Pressure, (b) Temperature, (c) Shear rate and (d) Viscosity distributions.

expected, the maximum temperature rise in this case is higher than for SRR=0.4 at just over 180 K (Fig. 15b) due to increased sliding. In addition, there is significant heating in the middle of the inlet region occurring due to forward heat conduction, which in turn leads to a lower viscosity in the inlet near the surface of the sliding wall. Overall, the maximum viscosity rise is less than for SRR=0.4, with the maximum being 658 Pa s at a location near the lower stationary surface (Fig. 15d). This coincides with the regions of low shear rates and temperatures (Fig. 15c and b). There is a considerable amount of shear-thinning in the middle of the contact, where both the temperature and shear rates are elevated. Maximum shear rate occurs on the stationary surface near the constriction, but there is also a second local maximum here at the surface of the moving wall towards the contact inlet.

It should be noted that the flat central region typical of high pressure EHL contacts is not evident in Figs. 14 and 15, despite the maximum pressure reaching as high as 1.6 GPa, due to the very high reduced modulus and hence, relatively small elastic deformations. To illustrate this, Fig. 16 shows a series of example solutions with reduced contact modulus being either, E_r=345.23 GPa in Fig. 16a and c (the wall remains rigid as in Fig. 14 an 15 but the cylinder modulus is now 100 GPa instead of 200 GPa i.e. equivalent to a steel on steel contact) or E_r=690.46 GPa in Fig. 16b (rigid wall, and cylinder modulus of 200 GPa i.e. twice the stiffness of a steel on steel contact). The load is also varied from 40 kN/m to 600 kN/m. The flat region is clearly apparent for cases of E_r=345.23 GPa (Fig. 16a and c) as may be expected, and is not evident in Fig. 16b corresponding to a high stiffness, low load contact. In addition, the maximum pressure in Fig. 16a is shown to reach 4 GPa. In terms of the dimensionless EHL parameters, $\overline{U}$, $\overline{W}$and$\overline{G}$, defined earlier in this section, the conditions shown in Fig. 16 and elsewhere in this paper span the following range: $\overline{U} = 5.69.10^{-12}$ (Figs. 10, 12 and 16c) to $\overline{U} = 1.14.10^{-9}$ (Fig. 16a), $\overline{W} = 9.1.10^{-6}$ (Fig. 16b) to $\overline{W} = 2.7.10^{-4}$ (Fig. 16a) and $\overline{G} = 3.86.10^{3}$ (Fig. 16c) to $\overline{G} = 13.7.10^{3}$ (Figs. 14 and 15). The maximum values of $\overline{W}$and$\overline{G}$ are much larger than those employed, for example, by Hartinger et al. [20] (achieved here by increasing the load and the elastic modulus of the cylinder respectively) which illustrates the improved stability of the present model. The stated values of $\overline{G}$ and $\overline{W}$ also help to explain why the elastic deformation of the cases shown in Fig. 16a and c is larger than that for the cases of Figs. 14 and 15.

It should be noted that although the results presented in this section assume a conductive cylinder and a constant temperature moving wall, boundary condition shown to be representative of a range of sliding-rolling contacts, including cases where the cylinder may be stationary (but not were the wall is stationary), the model is capable of dealing with both solid bodies being conductive. To illustrate this, Fig. 17 shows the temperature distribution for the sliding-rolling case shown in Fig. 14 above where both bodies are conductive and heat transfer is solved throughout. It is evident that under these conditions

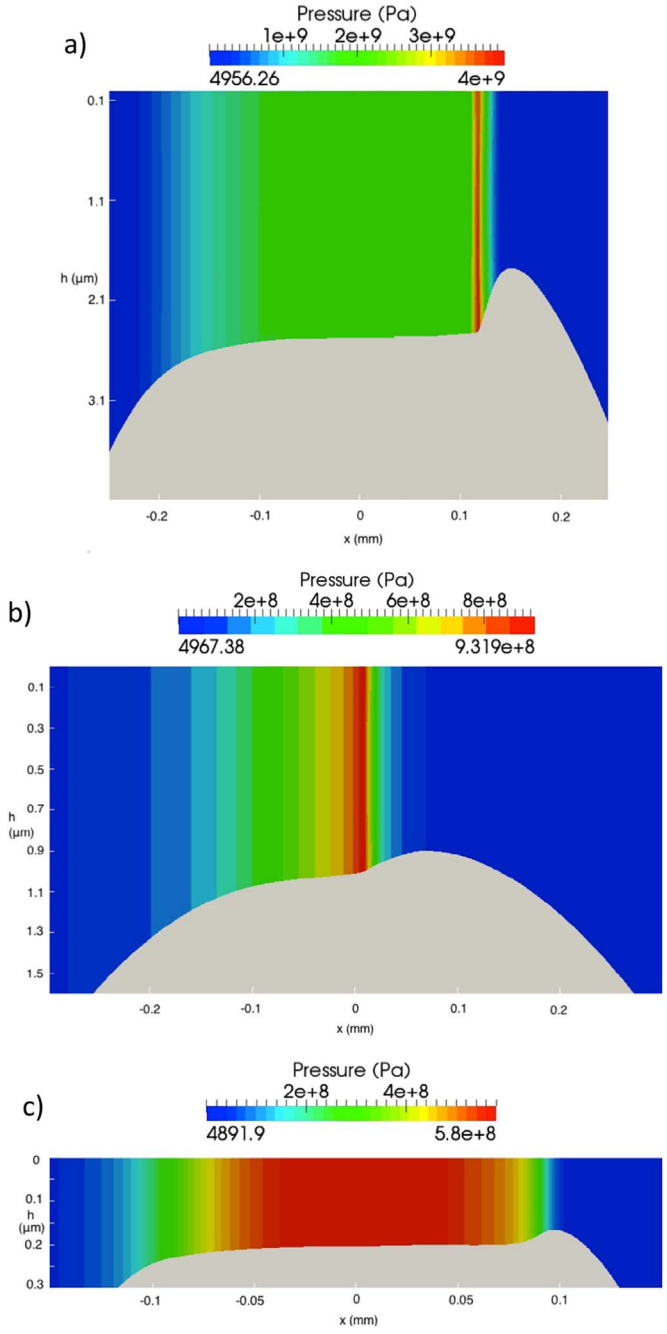

Fig. 16. Pressure predictions from the full thermal CFD model a) U_e=2.5 m/s, SRR=0, η_0=1.0 Pa s, E_r=345.23 GPa, Converged load =600 kN/m; b) U_e=2.5 m/s, SRR=0, η_0=0.04 Pa s, E_r =690.46 GPa, Converged load =40 kN/m; c) Isothermal solution, U_e=2.5 m/s, SRR=2, η_0=0.01 Pa s, E_r=345.23 GPa, Converged load=100 kN/m.

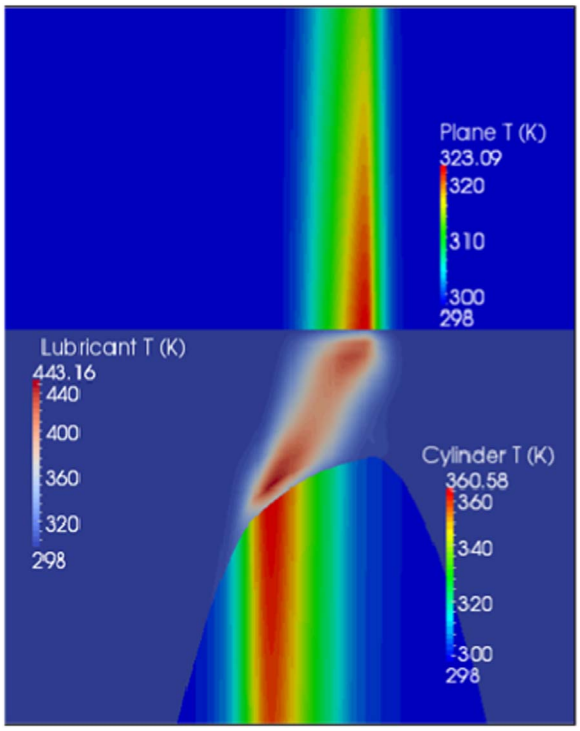

Fig. 17. Temperature distribution with both solids being conductive and having thermal properties shown in Table 3. The same case as that shown in Fig. 14 above (U_e=2.5 m/s, SRR=0.4, η_0=0.5 Pa s, E_r=690.46 GPa, Converged load=420 kN/m); Length scales are the same as those shown in Fig. 14b.

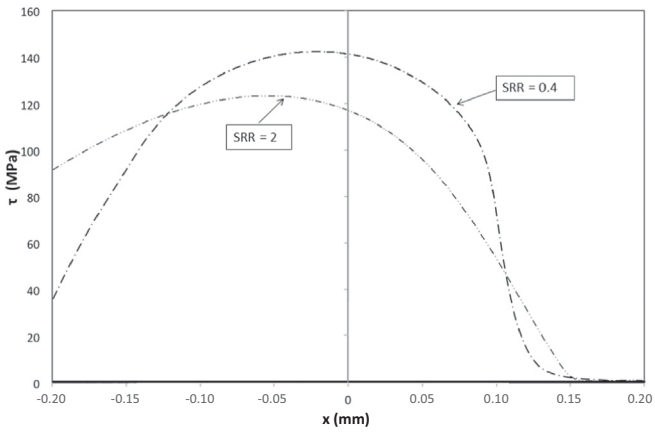

Fig. 18. Predicted shear stress distributions along the top sliding wall for pure sliding (SRR=2, converged load=400 kN/m) and sliding-rolling case (SRR=0.4, converged load =420 kN/m)); (CFD thermal solution, U_e=2.5 m/s, η_0 =0.5 Pa s, E_r=690.46 GPa.

(SRR=0.4) the lubricant temperature distribution and absolute values are very similar to those predicted previously (Fig. 14b). This is not surprising since under rolling-sliding contact conditions as shown in this study, the faster body (in this case the cylinder) will absorb most of the heat generated in the contact. In contrast, where the wall itself is near stationary (not studied here), both the cylinder and the wall should ideally be considered as conductive solids.

3.5. Contact shear stress and friction

One of the important benefits offered by the current model is its ability to accurately predict friction forces in an EHL contact for given loading conditions and lubricant properties, subject to appropriate rheology laws for the given fluid being implemented. This makes it a powerful tool for improving operational efficiency through the optimisation of contact in terms of lubricant properties for given contact conditions. Hartinger et al. [20] used their model to compare predicted shear stresses, and resulting friction coefficients for a range of slide-roll ratios. When full thermal analysis was conducted they found that higher slide roll ratios reduced friction, due to the increase in lubricant temperature and the associated drop in viscosity. However, their model was only capable of dealing with relatively low pressures and therefore it is interesting to consider whether the same trend is valid at higher pressure levels that can be reached by the current model. To this effect, Fig. 18 shows the values of the shear stress along the rigid wall for the two cases considered in Figs. 14 and 15 with SRR=0.4 and SRR=2 respectively. It is evident that the pure sliding case produces lower

maximum shear stress than the sliding–rolling case (SRR=0.4) under these conditions. The predicted drop in the shear stress level, and therefore friction force, is due to higher lubricant temperature in the case of pure sliding. The trend observed by Hartinger et al. [20] at lower pressure levels therefore holds at these higher pressures too.

4. Conclusion

This paper presents a new numerical methodology for modelling elasto-hydrodynamic lubrication where the finite volume approach is used for the numerical solution of the governing equations for both fluid and solid domains, resulting in a partitioned two-way-strongly-coupled FSI model. The model is implemented in an open source CFD package, OpenFOAM. Two-way coupled finite volume approach and implementation of efficient numerical algorithms ensures that model remains stable over a wide range of conditions including high deformations and contact pressures of over 3 GPa. This makes the model applicable to practical EHL contacts such as those found in rolling element bearings.

Solution of full Navier-Stokes equations in the fluid domain and the Navier-Lamé equation in the solid domain provides a more physical representation of the EHL contact that is able to deal with non-Newtonian fluid effects, cavitation and arbitrary contact geometry. Thermal effects are dealt through the solution of the energy equation. Fluid cavitation is accounted for by using a homogenous equilibrium cavitation model, which imposes the specified saturation pressure inside the cavitating region.

Notwithstanding the improved physical representation of the EHL contact, accuracy of the model predictions is of course dependant on the validity of the implemented rheological laws. The methodology presented in this paper is suitable for the implementation of any desired rheological relationships, but these need to be known in advance.

Results are presented to validate the model predictions against existing EHL models based on both Reynolds and CFD methods within the range of conditions where these exiting solutions are valid. Further results are then shown for a range of conditions, including higher pressures, and different slide-roll ratios, elastic properties and fluid viscosities, to illustrate the overall stability and capabilities of the model. An example case is also shown to illustrate that the proposed CFD approach is capable of capturing EHL contact phenomena beyond that accounted for by standard Reynolds-based approaches. However, this improvement in accuracy comes at a considerably higher computational cost, so that the use of the proposed method, in line with other CFD approaches, is only justifiable in cases where the Reynolds-based approaches may not be suitable, particularly under severe contact conditions and where the full thermal solution of an EHL problem may be required.

Acknowledgements

The authors thank the SKF Engineering and Research Centre for providing financial support for this work via the SKF University Technology Centre in Advanced Modelling and Measurements in Tribology at Imperial College London. D.D. would also like to acknowledge the support received from the EPSRC under the Established Career Fellowship grant EP/N025954/1. All data and results are made available upon request by email to the corresponding author or tribology@imperial.ac.uk.

References

[1] Tower B. First report on friction experiments (friction of lubricated bearings). Proc Inst Mech Engeneers 1883:632–59.
[2] Grubin AN, Vinogradova IE, Ketova KF. Fundamentals of the hydrodynamic theory of lubrication of heavily loaded cylindrical surfaces. Investigation of the Contract of Machine Components. Central Scientific Research Institute for Technology and Mechanical Engineering; 1949.
[3] Gohar R, Cameron A. Optical measurement of oil film thickness under. Nature 1963;200(4905):458–9.
[4] Reynolds O. On the Theory of lubrication and its application to Mr. Beauchamp Tower's experiments, including an experimental determination of the viscosity of olive oil. In: Proceedings of The Royal Society of London. vol. 40(242–245); 1886. p. 191–203.
[5] Cameron A, Wood WL. The full journal bearing. Proc Inst Mech Eng 1949;161(1):59–72.
[6] H. Sassenfeld and A. Walther, Gleitlagerberechnungen, VDI-Forschungsheft, Vol. 441, 1954.
[7] Dowson D, Higginson GR. A numerical solution to the elasto-hydrodynamic problem. J Mech Eng Sci 1959;1(1):6–15.
[8] Dowson D, Toyoda S. A central film thickness formula for elastohydrodynamic line contacts. In: Proceedings of the 5th Leeds-Lyon symposium on tribology; 1978. p. 60–5.
[9] Hamrock BJ, Dowson D. Ball bearing lubrication: the elastohydrodynamics of elliptical contacts. New York: John Wiley & Sons; 1981.
[10] Johnson KL, Tevaarwerk JL. Shear behaviour of elastohydrodynamic oil films. Proc R Soc Lond A Math Phys Sci 1977;356(1685):215–36.
[11] Najji B, Bou-Said B, Berthe D. New formulation for lubrication With non-Newtonian fluids. J Tribol 1989;111(1):29–34.
[12] Conry TF, Wang S, Cusano C. A Reynolds-Eyring equation for elastohydrodynamic lubrication in line contacts. J Tribol 1987;109(4):648–54.
[13] Schäfer CT, Giese P, Rowe WB, Woolley NH. Elastohydrodynamically lubricated line contact based on the Navier-Stokes equations. In: Dowson D, editor. Tribology series. The Netherlands: Elsevier; 2000. p. 57–69.
[14] Bair SS. High pressure rheology for quantitative elastohydrodynamics. Tribology and interface engineering series, 54. The Netherlands: Elsevier Science; 2007.
[15] Keogh PS, Gomiciaga R, Khonsari MM. CFD based design techniques for thermal prediction in a generic. J Tribol 1997;119(3):428–35.
[16] Tucker PG, Keogh PS. On the dynamic thermal state in a hydrodynamic bearing with a whirling journal using CFD techniques. J Tribol 1996;118(2):356–63.
[17] Almqvist T, Larsson R. The Navier–Stokes approach for thermal EHL line contact solutions. Tribol Int 2002;35(3):163–70.
[18] Hamrock BJ, Schmid SR, Jacobson BO. Fundamentals of fluid film lubrication. New York: Marcel Dekker; 2004.
[19] Almqvist T, Almqvist A, Larsson R. A comparison between computational fluid dynamic and Reynolds approaches for simulating transient EHL line contacts. Tribol Int 2004;37(1):61–9.
[20] Hartinger M, Dumont M-L, Ioannides S, Gosman D, Spikes H. CFD modeling of a thermal and. J Tribol 2008;130(4), [p. 041503-041503].
[21] Bruyere V, Fillot N, Morales-Espejel GE, Vergne P. Computational fluid dynamics and full elasticity model for sliding line thermal elastohydrodynamic contacts. Tribol Int 2012;46(1):3–13.
[22] ⟨http://openfoam.com/documentation/user-guide/⟩.
[23] Moukalled F, Mangani L, Darwish M. The finite volume method in computational fluid dynamics: an advanced introduction with OpenFOAM® and Matlab. Switzerland: Springer International Publishing; 2015.
[24] Weller H. User Guide. OpenCFD limited; 2004. ⟨http://www.openfoam.com/⟩.
[25] Dowson D, Higginson GR. Elasto-hydrodynamic lubrication. Oxford: Pergamon Press; 1977.
[26] D. Dowson and C.M. Taylor, Fundamental aspects of cavitation in bearings. In: Proceedings of the 1st Leeds Lyon symposium on tribology, 1974. pp. 15–26.
[27] Wu SR. A penalty formulation and numerical approximation of the Reynolds-Hertz problem of elastohydrodynamic lubrication. Int J Eng Sci 1986;24(6):1001–13.
[28] Hartinger M. CFD modelling of Elastohydrodynamic lubrication, inMechanical Engineering. United Kingdom: Imperial College London; 2007.
[29] Dowson D. A generalized Reynolds equation for fluid-film lubrication. Int J Mech Sci 1962;4(2):159–70.
[30] Haosheng C, Darong C. Modified Reynolds equation for Non-Newtonian fluid with rheological model in frequency domain. J Tribol 2005;127(4):893–8.
[31] Peiran Y, Shizhu W. A generalized Reynolds equation based on non-Newtonian flow in lubrication mechanics. Acta Mech Sin 1990;6(4):289–95.
[32] Wolff R, Kubo A. A generalized non-Newtonian fluid model incorporated into elastohydrodynamic lubrication. J Tribol 1996;118(1):74–82.
[33] Roelands CJA. Correlational aspects of the viscosity-temperature pressure relationship of lubricating oils. The Netherlands: Technical Universty of Delft; 1966.
[34] Houpert L. New results of traction force calculations in elastohydrodynamic contacts. J Tribology 1985;107(2):241–5.
[35] Bair S. A note on the use of Roelands equation to describe viscosity for EHD Hertzian zone calculations. J Tribol 1993;115(2):333–4.
[36] Bair S. The variation of viscosity With temperature and pressure for various real lubricants. J Tribol 2000;123(2):433–6.
[37] Kauzmann W, Eyring H. The viscous flow of large molecules. J Am Chem Soc 1940;62(11):3113–25.
[38] Cheng HS. A refined solution to the thermal-elastohydrodynamic lubrication of rolling and sliding cylinders. ASLE Trans 1965;8(4):397–410.
[39] Cheng HS, Sternlicht B. A numerical solution for the pressure, temperature, and film thickness between two Infinitely long, lubricated rolling and sliding cylinders, under heavy loads. J Basic Eng 1965;87(3):695–704.
[40] Zhu D, Wen SZ. A full numerical solution for the thermoelastohydrodynamic problem in elliptical contacts. J Tribol 1984;106(2):246–54.
[41] Kim KH, Sadeghi F. Three-dimensional temperature distribution in EHD lubrication: Part I—circular contact. J Tribol 1992;114(1):32–41.

[42] Wang S, Conry TF. Thermal non-Newtonian elastohydrodynamic lubrication of line contacts under simple sliding conditions. ASME J Tribol 1992;114:317.
[43] Conry TF. Thermal effects on traction in EHD lubrication. J Lubr Technol 1981;103(4):533–8.
[44] Wang S, Cusano C, Conry TF. Thermal analysis of elastohydrodynamic lubrication of line contacts using the Ree-Eyring fluid model. J Tribol 1991;113:232–42.
[45] Yang P. On the transient thermal elastohydrodynamic lubrication. China: Tsinghua University; 1989.
[46] Habchi W, Eyheramendy D, Bair S, Vergne P, Morales-Espejel G. Thermal elastohydrodynamic lubrication of point contacts using a Newtonian/generalized Newtonian lubricant. Tribol Lett 2008;30(1):41.
[47] Habchi W, Eyheramendy D, Vergne P, Morales-Espejel G. Stabilized fully-coupled finite elements for elastohydrodynamic lubrication problems. Adv Eng Softw 2012;46(1):4–18.
[48] Jasak H, Weller HG. Application of the finite volume method and unstructured meshes to linear elasticity. Int J Numer Methods Eng 2000;48(2):267–87.
[49] Ferziger JH, Peric M. Computational Methods for Fluid Dynamics Springer Berlin Heidelberg; 2001.
[50] Blom FJ. Considerations on the spring analogy. Int J Numer Methods Fluids 2000;32(6):647–68.
[51] Jasak HT, Tukovic Z. Automatic mesh motion for the unstructured finite volume method. Trans FAMENA 2006;30(2):1–20.
[52] Benra FK, Dohmen HJ, Pei J, Schuster S, Wan B. A comparison of one-way and two-way coupling methods for numerical analysis of fluid-structure interactions. J Appl Math 2011;2011:16.
[53] Bertocchi L, Dini D, Giacopini M, Fowell MT, Baldini A. Fluid film lubrication in the presence of cavitation: a mass-conserving two-dimensional formulation for compressible, piezoviscous and non-Newtonian fluids. Tribol Int 2013;67:61–71.
[54] Giacopini M, Fowell MT, Dini D, Strozzi A. A mass-conserving complementarity formulation to study lubricant films in the presence of cavitation. J Tribol 2010;132(4), [p. 041702-041702].
[55] Liu X, Jiang M, Yang P, Kaneta M. Non-Newtonian thermal analyses of point EHL contacts using the Eyring model. J Tribol 2005;127(1):70–81.